A Dimensionless Number for High-throughput Design of Multi-Principal

Element Alloys in Directed Energy Deposition

Zahabul Islam, Phalgun Nelaturu, Dan J. Thoma^{a)}

AFFILIATIONS

Alloy Design and Development Laboratory, Department of Materials Science and Engineering,

University of Wisconsin, Madison, WI 53706, USA

a) Author to whom correspondence should be addressed: dthoma@wisc.edu

ABSTRACT

The present study demonstrates the development of a dimensionless number to predict the build height

in the additive manufacturing technique of directed energy deposition (DED). The build height also can

be used to estimate the dendrite arm spacing, and thus the cooling rate, in the fabrication of samples. A

baseline sample, 316L stainless steel, was used to fit the build height to the dimensionless number. A

range of process parameters, including laser power, laser feed rate, powder flow rate, layer thickness,

and hatch spacing were varied. Based upon dendrite arm spacing, the estimated cooling rate varied

between 10²-10⁴ K/s. Using the fitted relationship for the stainless steel, high-throughput (HT)

processing of multi-principal element alloys (MPEAs) was performed. For this study, HT is the ability

to fabricate a batch of 25 bulk samples (~ 1 cm³) with different compositions within a five-hour period

with +/- 10 at.% accuracy. A range of compositions using in situ alloying of elemental powders in the

Fe-Ni-Cr-Mo system were made. The MPEAs' build height followed the same relationship to the

dimensionless number as the 316L alloy. The dimensionless number predicts both macro and meso-

scale features in HT processing, thus offering a design tool for choosing process parameters in DED

additive manufacturing. Also, the ability to control or increase cooling rates can enhance the ability to

promote metastability, as well as control the meso-scale chemical distributions of the alloy samples.

Keywords: Dimensionless number, Metastability, Additive manufacturing

1

Multi-principal Element Alloys (MPEAs), exist in large compositional spaces. With a potential compositional space of 5 to 35 atomic percent for each element, the number of possible alloy variations can include approximately 1 million distinct alloys for a five-component system [1-4]. Designing alloys in this large compositional space is challenging. Thermodynamic calculations can provide insight into equilibrium phase boundaries [5-8], but available databases can limit the predictions. Thus, high-throughput (HT) methods to fabricate samples are required to characterize and validate predictions as well as test properties and build databases in MPEA compositional space.

The HT fabrication methods of bulk, condensed inorganic samples at elevated temperatures are arguably in its infancy. Although HT or combinatorial methods exist and can facilitate testing and database development, bulk sample fabrication methods have been limited. Recently, Directed Energy Deposition (DED) has been demonstrated as a HT fabrication method for bulk alloy production [9-11]. This process consists of varying the flow rate of powders from up to four hoppers, where the powders blend in a carrier gas and are distributed from a nozzle (Fig. 1). The stream of powders intersects with a laser, permitting *in situ* alloying. With calibrated flow rates, compositional changes can be made, and 25 compositions of roughly 1 cm³ specimens can be fabricated within a five-hour period. However, the challenge of this HT manufacturing is the ability to predict the process conditions without trial and error.

Laser-based additive manufacturing techniques, in general, have high cooling rates. The small focal point of the moving laser (typically less than 1 mm) and the associated small molten volumes on a larger cooled heat sink provides high cooling rates from $10^2 - 10^6$ K/s, with DED methods having cooling rates in the lower half of this range [12-15]. For alloys, and in particular MPEA sample fabrication, the high cooling rates associated with the DED process help reduce microsegregation, with the potential to exhibit non-equilibrium solidification and retention of metastable phases. MPEAs are often characterized as exhibiting sluggish diffusion [16,17], so the reduced scale of dendritic microsegregation will either decrease required homogenization times or enable metastability for enhanced properties or functionality [18-21].

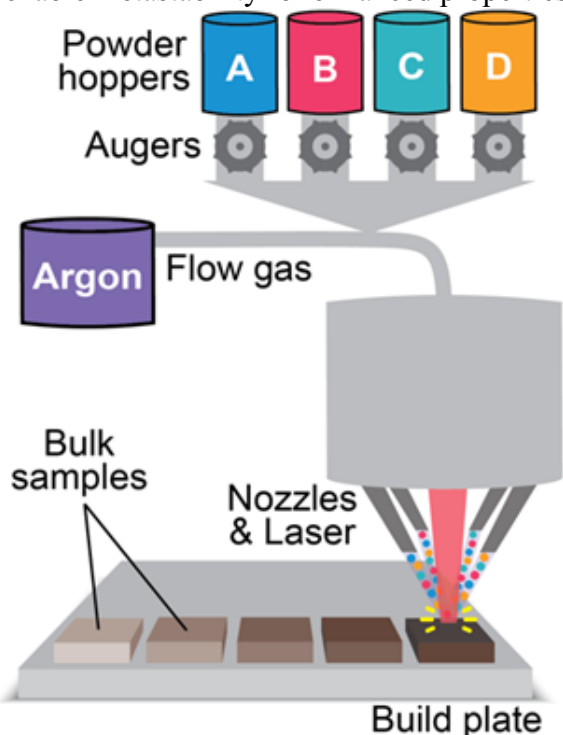


FIG. 1. Schematic of the DED process for HT fabrication of 1 cm³ samples with different compositions.

This study proposes a design strategy for the HT fabrication of MPEAs. Using the proposed methodology, unknown process parameters can be defined for a new material. Moreover, tailoring the cooling rate to increase the metastability is included to facilitate MPEAs fabrication and increase the potential of metastability in the fabricated samples. Linking two length scales (macro-and meso-scale) offers a useful method in the design process. A dimensionless number is proposed to provide a mass and energy balance approximation to predict the processing of alloys in the DED process.

While dimensionless numbers are widely used in fluid mechanics, their use in additive manufacturing (AM) is still under development. A dimensionless number is expressed by a group of parameters, related to the process as well as inherent to the material, and could be effectively utilized to study additive manufacturing processes [22-24]. The advantages of using a dimensionless number in additive manufacturing techniques can be found elsewhere [24,25]. In this study, a dimensionless number has been developed for directed energy deposition (DED) as a function of process parameters such as laser power, laser spot size, feed rate (laser traverse speed), layer thickness, hatch spacing, and mass flow rate as well as materials properties such as thermal diffusivity, specific heat capacity, latent heat of fusion, and melting point. To accomplish this goal, the Buckingham PI theorem [26] has been applied to derive a relationship among process as well as machine parameters and properties of interest. Assuming physical and geometric properties are a strong function of global energy density, E_g , the dimensionless number, Π , can be written in the following form (the definitions and form of the terms in the equation are given in TABLE I. below):

$$\Pi = \mathcal{E}_{\mathbf{g}}\{\mathbf{H}\}^{\mathbf{a}} \{\alpha\}^{\mathbf{b}} \{\dot{\mathbf{m}}\}^{\mathbf{c}} \tag{1}$$

TABLE I. The definition of the parameters and their dimensions used in Eq. (1) are shown in the following table:

Parameters	Expression	Dimensions	
Global energy density	$E_g = P/vD_l$	MT^{-2}	
Thermal diffusivity	$\alpha = k/\rho C_p$	L^2T^{-1}	
Latent heat of fusion and sensible heat	$H = H_f + C_p \times (T_m - T_o)$	L^2T^{-2}	
Mass flow rate	ṁ	MT^{-1}	

where P, v, D_l , α , k, ρ , C_p , H, H_f , T_m , T_o and \dot{m} are laser power, feed rate, laser spot diameter, thermal diffusivity, thermal conductivity, density, specific heat capacity, latent heat, latent heat of fusion, melting temperature, ambient temperature, and mass flow rate, respectively. Global energy density, E_g , can be defined as the ratio of laser power to the feed rate times laser spot size [27] as shown in Table I.

Using the Buckingham PI theorem in Eq. (1), a dimensionless number can be derived as follows:

$$\Pi_1 = \frac{E_g \times \alpha}{\dot{\mathsf{m}} \times \mathsf{H}} \tag{2}$$

In this study, four variables (i=4) namely, E_g , α , H, and m were chosen and three dimensions were involved [M, L, and T] (j=3). Thus, according to Buckingham PI theorem [26], at least one dimensionless number, $\Pi \le i$ -j = 4-3 = 1 can be developed. The dimensionless number expressed by the Eq. (2) represents the ratio of input laser energy to melt the material with respect to heat dissipation. However, in a DED system, the choice of layer thickness and

hatch spacing is dictated by the laser power and laser spot size. In addition, properties such as density and build height are also influenced by layer thickness (Z) and hatch spacing (h). The melt pool dimensions are dictated by the laser power, feed rate, and laser spot size. At a constant laser power and feed rate, if the hatch spacing is larger than the melt pool width, then overlap of the melted regions will be incomplete and a poor build. If the layer thickness is higher than the melt pool depth, delamination will take place between the layers. Hence, a relationship is required to avoid these types of defects in the printed components. Thus, at a constant energy density the layer thickness and hatch spacing could not be arbitrarily chosen. To accommodate this effect in this study, a dimensionless length ($L^* = Z/h$) which is a ratio of layer thickness to hatch spacing was introduced into Eq. (2). The addition of the dimensionless length is expressed in Eq. (3) as follows:

$$\Pi_2 = \frac{E_g \times \alpha}{m \times H} \times \frac{Z}{h} \tag{3}$$

Based upon a Rosenthal temperature distribution simulation [28], laser spot size can be correlated with layer thickness and hatch spacing. A range of values for layer thickness and hatch spacing are recommended as follows:

$$0.4D_l \le Z \le D_l \tag{4a}$$

$$0.4D_l \le h \le 0.6D_l \tag{4b}$$

The dimensionless number described in Eq. (3) can be applied for both pre-alloyed powders as well as *in situ* alloying of multi-component alloys such as MPEAs. In general, the number is a mass and energy balance of the processing conditions and thermophysical properties of the materials. In the case of all alloys, properties can be evaluated by taking averages as described in Eq. (5).

$$S = \sum_{i} x_i N_i \tag{5}$$

where S is the property of interest used in Eq. (5), x_i , N_i are the atom percentage and property of interest of the ith element, respectively. The dimensionless number demonstrated by Eq. (3) was used to develop relationships among measured physical properties as well as physical dimensions. Specifically, the dimensionless number was used to express the physical dimension of build height. To demonstrate the application of this concept, 316L stainless steel (SS) and a range of compositions within the MPEA system of Cr, Fe, Ni, and Mo were processed. Materials properties [29] are listed in TABLE II as follows.

TABLE II. Physical properties of materials used in this study:

Properties	Cr	Fe	Ni	Mo
$\alpha \text{ (mm}^2/\text{s)}$	29.18	22.34	22.6	53.8
$H_{f}(kJ/kg)$	394.26	247.11	293.05	375.2
C _p (kJ.kg ⁻¹ .K ⁻¹)	0.448	0.449	0.445	0.251
$T_{m}\left(K\right)$	2180	1811	1728	2896

The DED machine used in this study was an Optomec LENS MR-7. Spherical, gasatomized 316L stainless steel powder in the size range 45µm - 150µm (purchased from Stanford Advanced Materials) was filled in one of the four hoppers connected to the LENS MR-7. Ar flow gas brought the powder from the hoppers into the path of the 1kW Nd:YAG 1070 nm wavelength laser with a 600 µm spot size and melted and deposited on the 316L SS build plate. The mass flow rate of the powder was controlled by changing the RPM of the auger attached to the hopper. As defined above, in additive manufacturing, the melt pool geometry dictates the required hatch spacing and layer thickness. In the DED process, the melt pool is defined by the power, velocity, and powder feed rate [30]. Thus, the following process parameters were varied to analyze the variation of build heights – laser power (P), feed rate (v), powder mass flow rate (m), laser hatch spacing (h), and layer thickness (Z). The scan strategy was kept constant for all samples – a bi-directional, single pass of laser beam for each print layer and a 90° rotation of scan vector for each subsequent layer. Although scan strategy will affect the heat transfer and therefore affect the melt pool geometry, defining a stable build at a constant scan strategy is a required first step. Each sample was printed for 10 layers with each print layer being square shaped with dimensions 6.35 mm x 6.35 mm. During the printing, the stand-off distance (i.e., the distance between the nozzle tip and build plate) was set to 9.53 mm. The range of the process parameters used in this study are described in TABLE III. For 316L SS, laser powers were varied from 200 to 600W in increments of 100W, the layer heights were varied from 0.25 to 1.25 mm in increments of 0.25 mm, hatch spacings were varied from 0.25 to 0.51 mm in increments of 0.13 mm, and two laser feed rates of 6.35 mm/s and 10.58 mm/s were used. Each sample represented a unique process condition. Most 316L samples with a high heat input ($\Pi_2 > 80$) were rejected. Some of the process parameter combinations with high heat inputs ($\Pi_2 > 80$) had severe volatilization, and many of these prints had to be interrupted due to safety concerns. Because these samples were not printed for all 10 print layers, the build heights could not be compared to the other samples and hence, were rejected. For some other process parameters with high heat inputs ($\Pi_2 > 80$), the build had a non-uniform build shape, making the measurement of build height inaccurate and not reportable. Finally, some low heat input samples ($\Pi_2 < 20$) displayed irregular build morphologies, apparently owing to insufficient melting. Most of these were samples rejected.

TABLE III. Table showing the process parameters that were varied during the 3D printing of 316L stainless steel and MPEAs.

Alloy	Laser power (W)	Feed rate (mm/s)	Layer thickness (mm)	Hatch spacing (mm)	Mass flow rate (g/min)
316L SS	200-600	6.35-10.58	0.25-1.25	0.25-0.51	5-15
MPEAs	400-750	8.47	0.46-0.83	0.38	9.64-25.08

316L SS was chosen as the model system to first demonstrate the effectiveness of the dimensionless number. The units for global energy density, thermal diffusivity, mass flow rate, and enthalpy (Eq. (3)) were used as J/mm², mm²/s, g/s, and J/g, respectively to calculate the dimensionless number values described in Eqs. (2) and (3). A normalized build height vs dimensionless number relationship is shown in Fig. 2(a) for 316 L SS. A normalized build height was used as a convenient way to represent the build height, as it is the ratio of the printed sample height to the set height per unit powder flow rate. This normalized build height can be expressed as follows:

$$h^* = \frac{h_{actutal}}{(n \times Z) \times \dot{m}} \tag{6}$$

where h^* , $h_{actutal}$, n, Z and \dot{m} are the normalized build height, actual build height, number of layers printed, layer thickness, and mass flow rate, respectively. The actual build height is the height physically achieved from the deposition of a prescribed number of layers, whereas number of layers times layer thickness indicates set height at the beginning of the print. In Fig. 2(a), the build height increases with the dimensionless number, and this can be attributed to the increased amount of input power. In addition, a linear relationship between normalized build height and the dimensionless number has been fitted from the experimental observation and

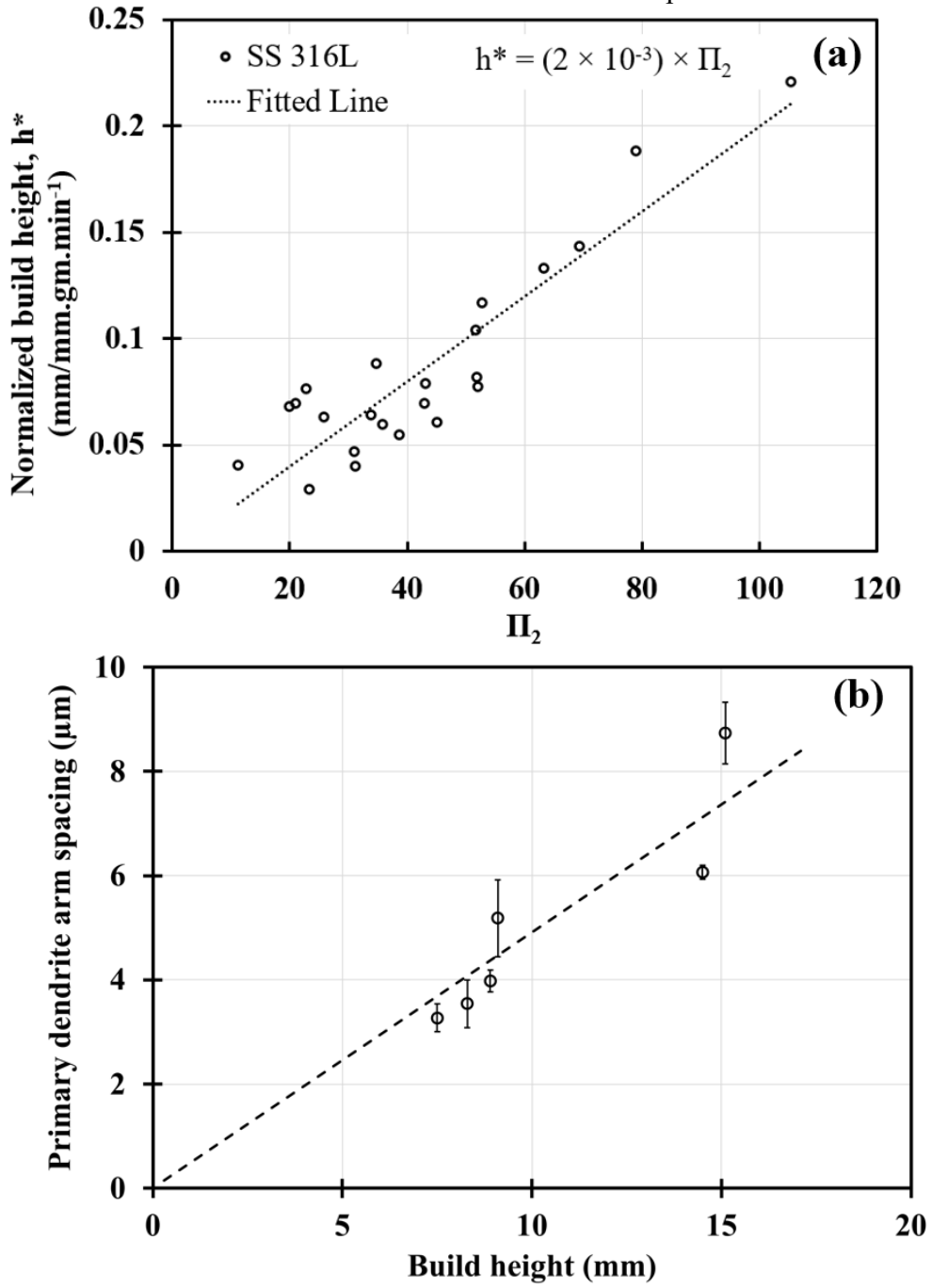


FIG. 2. (a) Normalized build height as a function of dimensionless number, and (b) Primary dendritic arm spacing as a function of actual build height. Trendlines through the origin are included.

can be expressed as:

$$h^* = 2.0 \times 10^{-3} \times \Pi_2 \tag{7}$$

Following the high-throughput (HT) analysis of build height, a few samples of the 316L SS were selected for low-throughput (LT) microstructural analysis. Since LT characterization is considerably more time-consuming, only a few samples at different dimensionless numbers were chosen to investigate the primary dendrite arm spacing (PDAS). Detailed studies of microstructural variation along the build direction in AM 316L samples have been previously reported [31]. In this work, the PDAS was measured half-way along the build height of each sample, in the center of melt pools. The plot in Fig. 2(b) depicts the relationship between PDAS and the build height used for the 316L SS samples. Most of the samples exhibited only primary dendrites. The cooling rate during the DED printing of these samples was high enough to suppress secondary dendrites from growing in most of the samples. Although PDAS is not a rigorous estimate of cooling rate in samples (compared to secondary dendrite arm spacing) [12,32,33], it is often used in the literature as a gauge of thermal history [13,34]. Nonetheless, the change of dimensions in the meso-scale are apparent. The DED-manufactured samples in the current study (Fig. 2(b)) exhibit primary dendritic arm spacing (PDAS) in the range 3.3±0.3 µm to 8.7±0.6 µm. This denotes a significantly slower cooling rate compared to the laser powder bed fusion (LPBF) manufactured 316L SS [34], but still fast enough to retard the growth of the secondary dendrites in most of the samples. The dendrite arm spacing values are also consistent with those reported in other studies [12,14,15], where observed dendrite spacings of ~ 3 µm estimated the cooling rate in DED to be around 10^3 - 10^5 K/s. For 316L SS, the relationship between PDAS (l_1) and cooling rate (e) is given by $l_1 = 80e^{-0.33}$ [13].

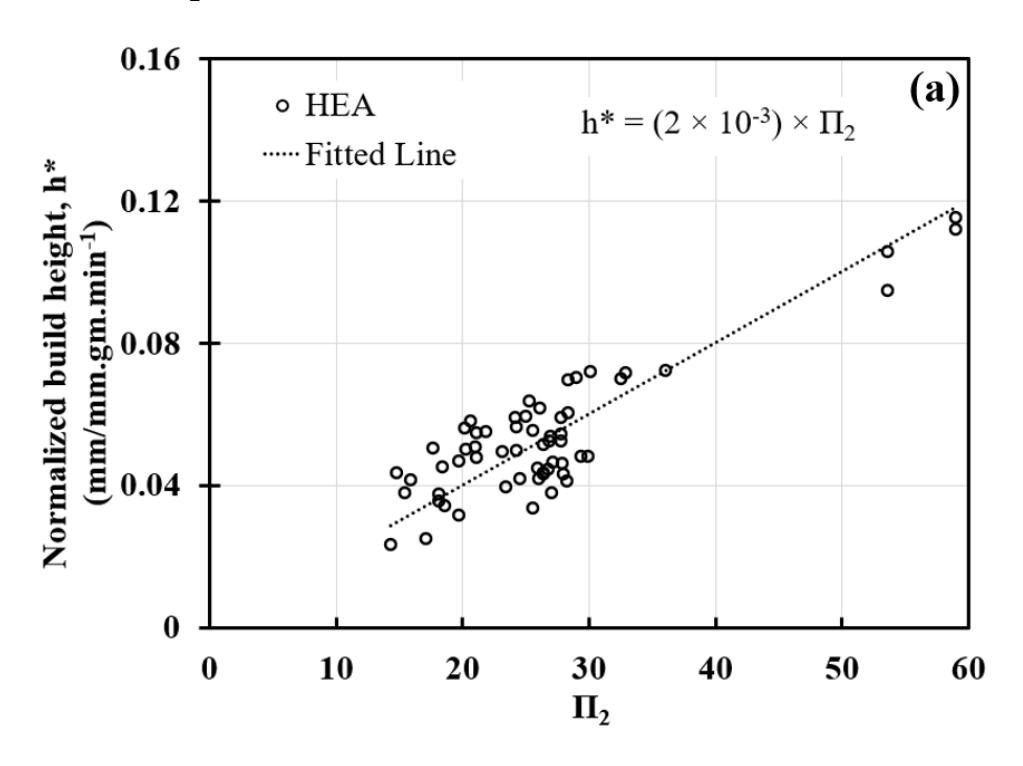
The significance of the use of the dimensionless number is two-fold. First, the dimensionless number provides a predictive means for the macro-scale build height, eliminating trial-and-error methods. In the DED process, the mass flow rate coupled with the process parameters dictates a specific layer height. For an effective build, the computercontrolled layer thickness increment of the working distance between the sample and laser/powder focal point must match the layer build height. If not, the laser focus will not be constant, resulting in an undesirable build. This relationship previously was defined through trial-and-error methods, whereas the proposed dimensionless number minimizes the time for process parameter optimization with a predictive design tool for a calibrated system. In addition to the macro-scale build height, the dimensionless number permits an estimate of the microsegregation length scale and possibly cooling rate. The build height of a sample reflects the total mass and energy required for each layer in the build process. Thicker layers (and consequently higher build heights for a constant number of layer thickness increments) have lower cooling rates (and coarser microsegregation). Although further studies can help to refine that relationship, the predictive nature of the dimensionless number permits tailored cooling rates for an increased potential of metastability in DED processed materials.

After using the dimensionless number in predicting the DED-based AM of 316L SS, the methodology was extended to a Fe-Ni-Cr-Mo MPEA system. For the 3D printing, individual elemental powders of Cr, Fe, Mo, and Ni in the size range $45\mu m$ - $150\mu m$ (purchased from American Elements) were filled in each of the four separate powder hoppers. The main difference in this application is the fact that for 316L, the composition did not change. For the MPEA, a range of compositions was investigated which introduced some challenges. The individual elements in the powder mixture had quite different melting temperatures. Mo has the highest melting temperature of 2623 °C while Cr has the lowest boiling temperature of

2672 °C. Furthermore, Cr has a very high vapor pressure and tended to volatilize easily. Therefore, it became a challenge to melt Mo without boiling away the Cr. In addition to depleting Cr in the final build, the severe volatilization also led to surface roughness and porosities. This was tackled by using relatively low Π_2 values (which was done by keeping lower powers) during the printing step and incorporating a remelting laser pass after each print layer. This involved running the laser over the deposited layer without having any powders blowing. This step helped to melt any unmelted Mo in the final build. The powers used varied from 400W to 750W depending on the compositions - 50W increment for every 5 at% increase in Mo. The parameters used to synthesize the MPEAs are listed in Table III. The composition of the powder blend coming out of the nozzle and into the laser path was dictated by the independent control of the auger RPMs on each hopper. This immediate ability to change powder compositions facilitates in situ alloying in a high-throughput (HT) fashion (see schematic in Fig. 1). The feed rate and hatch spacing were kept constant at 8.47 mm/s (20 inch/min) and 0.38 mm (0.015 inch), respectively.

A relationship between the normalized build height of MPEAs and the dimensionless number is shown in Fig. 3(a). The linear fit in Fig. 3(a) can be expressed as follows:

$$h^* = 2.0 \times 10^{-3} \times \Pi_2 \tag{8}$$



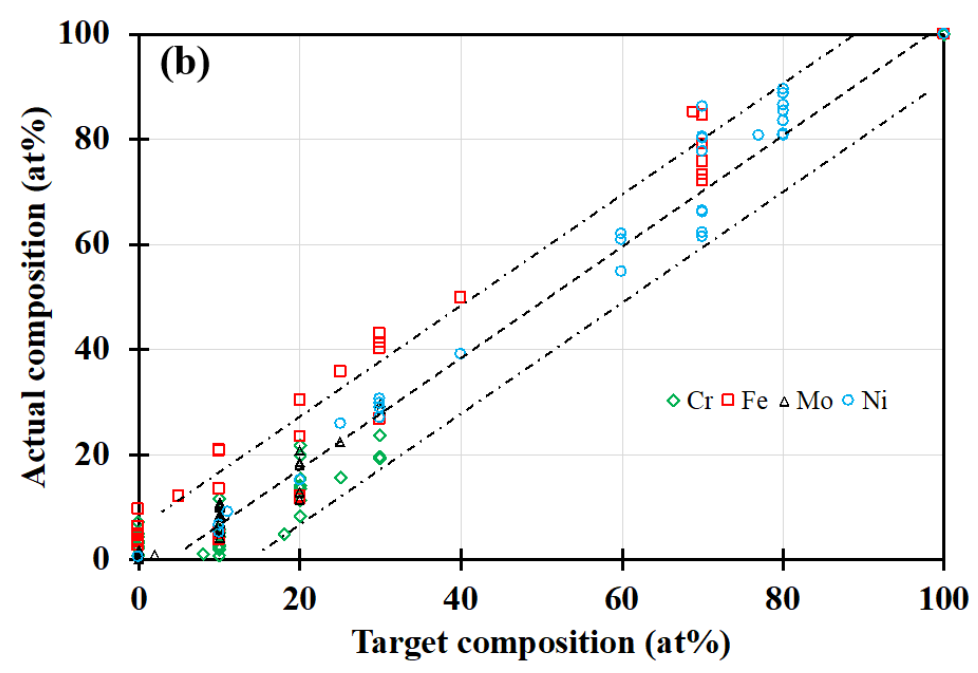


FIG. 3. (a) Normalized build height of MPEAs as a function of dimensionless number, and (b) the actual composition of the MPEAs compared to the intended compositions. The HT method, without optimization, permitted compositions within +/- 10 at.%.

This linear fit indicates that normalized build height for the MPEAs is the same as for 316L SS (in Eq. (6)), which supports that normalized build height of MPEAs can be predicted using the proposed dimensionless number. By following the linear fit in Eq. (8), the unknown process parameters of a material can be predicted. The details of the determination of unknown process parameters are explained in the supplementary section S1.

The actual vs. intended composition of the MPEAs is shown in Fig. 3(b). With a first level iteration, the compositions of the elements were within +/-10% as determined with X-ray fluorescence (XRF). The XRF scans were performed using a X-200 XRF Analyzer, a handheld instrument using a 40 kV, Rh anode source that enabled rapid composition measurement at the rate of 1 min/sample. A spot size of 3 mm diameter ensured that the measured compositions were averaged over a large enough sample surface area. The accuracy of the XRF measurements were calibrated using a 316L SS specimen whose actual compositions were measured by Luvak, Inc (the comparison is given in the supplementary material, Table S.II). The XRF-measured compositions were accurate to within ±0.3 wt%. Typically, errors in XRF measurements begin to increase for elements with atomic weights lower than aluminum. Since all the elements in the current alloy systems consisted of mainly transition elements or higher, XRF was a good high-throughput option to measure compositions. As can be seen, the printed alloy compositions span a significant portion of the compositional space – Fe varied 2-85 at%, Ni 0-100 at%, Cr 0-24 at%, and Mo 0-30 at%.

The dimensionless number proposed in this effort was effective in predicting the build height for both pre-alloyed 316L SS powder as well as for in situ alloying of elemental powder of an MPEA system. Although both systems contained the same constituent elements, this relationship did fit over a wide range of compositions with regression fits of R²=0.96. The comparison of all the data is shown in Fig. 4.

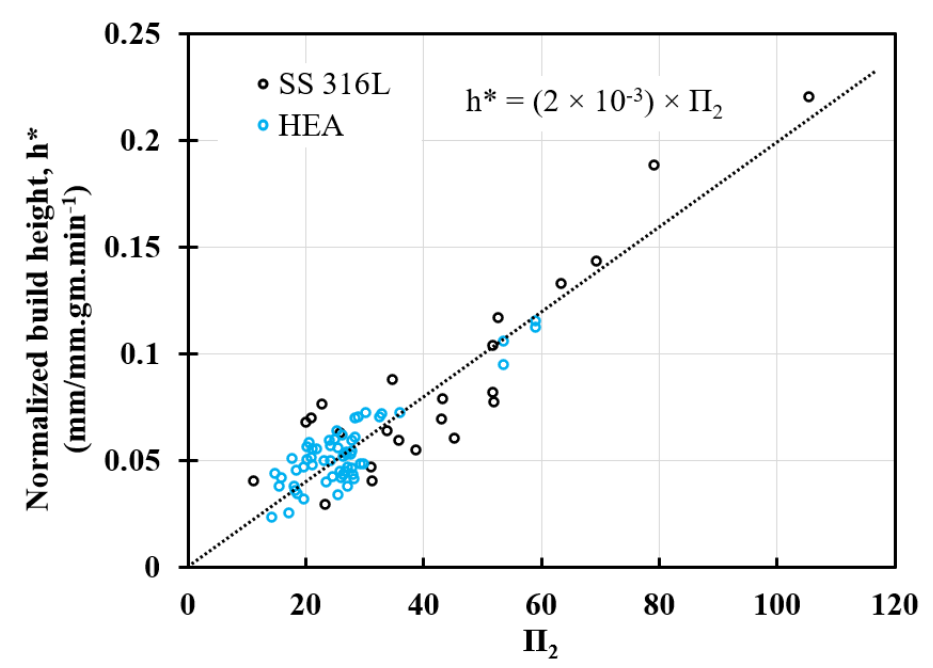


FIG. 4. Normalized build height of both 316L SS and MPEAs as a function of the dimensionless number.

A Zeiss LEO 1530 scanning electron microscope (SEM) was used for imaging and energy-dispersive spectroscopy (EDS). The phases present in all the alloy samples were measured via automated X-ray diffraction (XRD) in a Bruker D8 Discovery X-ray diffractometer (data provided in supplementary section S3). The micrographs in Fig. 5(a) and (b) show the microstructure of a single-phase FCC alloy of nominal composition $Fe_{60}Ni_{20}Cr_{10}Mo_{10}$ at two different magnifications., respectively. This MPEA was manufactured at a Π_2 value of 28 and built up to a height of ~3 mm. The microstructure consisted of only primary dendrites with no evidence of secondary dendrite formation. The PDAS in this alloy was quite fine and was measured to be $3.4\pm0.4~\mu m$, indicating a cooling rate of ~ $10^4~K/s$ based on the equation for 316L stainless steel cited previously. EDS area maps (Fig. 5(c) and (d)) of the sample surface corresponding to Fig. 5(b) depict the elemental distributions of Fe and Mo, respectively. The Mo segregated into the interdendritic regions, while the Fe was depleted in these regions. The Cr and Ni were distributed more uniformly throughout the microstructure. The Π_2 defined the parameters which controlled the cooling rate resulting in fine PDAS, and hence, a fine scale of microsegregation.

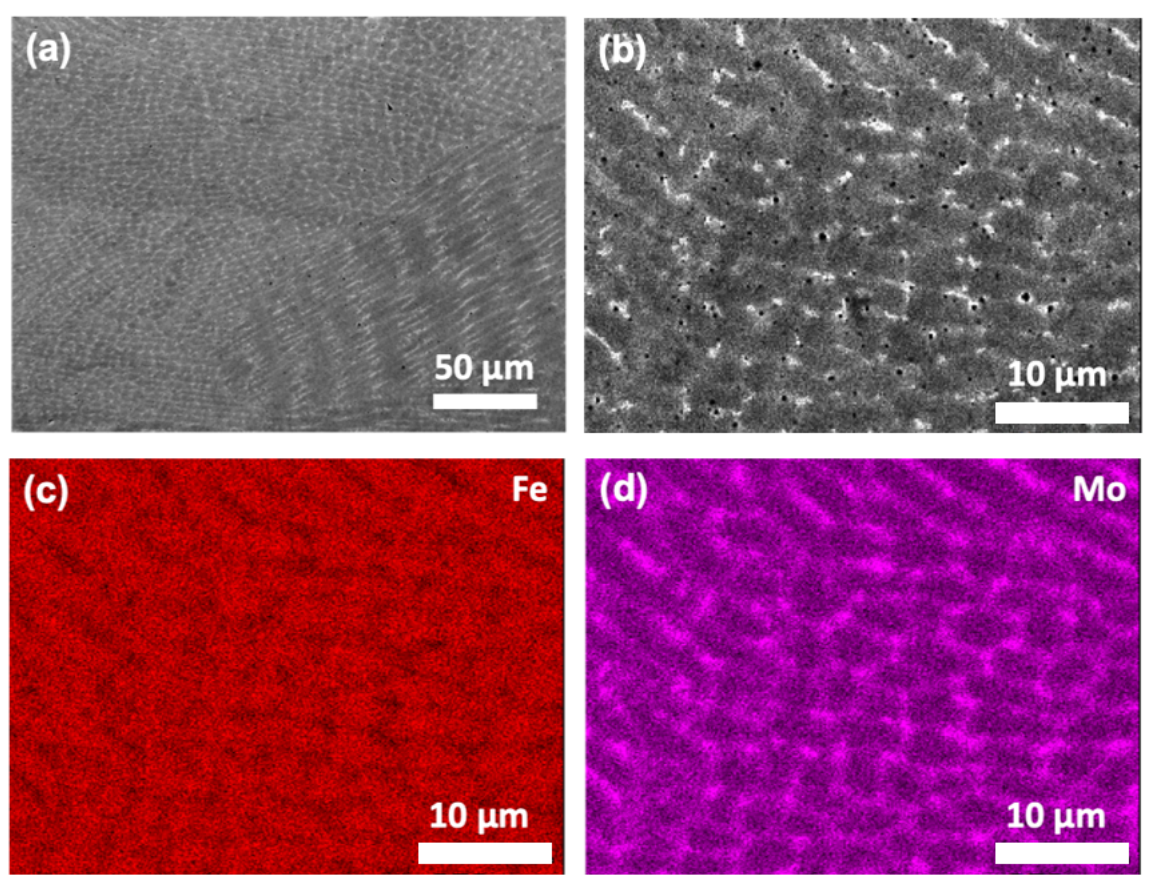


FIG. 5. (a) and (b) Microstructures of a Fe₆₀Ni₂₀Cr₁₀Mo₁₀ alloy, c) and d) EDS area maps corresponding to FIG. 5(b) depicting the Fe and Mo distributions, respectively.

The normalized build height as a function of the dimensionless number should be further investigated with different alloys systems. Furthermore, detailed investigations on the dendrite spacing as a function of the build heights are required. Nonetheless, the dimensionless number, based upon a mass and energy balance of the thermophysical properties with respect to the process parameters, permitted a reliable prediction of processing conditions for macroscale dimensional control. Meso-scale features such as dendrite arm spacing and microsegregation spacing can also be tailored with the term. The control of the dendrite arm spacing indicates the ability to tailor cooling rates that cover two orders of magnitude in the DED process, and thus provides a design parameter for promoting increased metastability. The dendrite arms spacings are typically five times finer than an arc-cast specimen, and the shorter distances of microsegregation allows shorter homogenization times during postprocessing. Finally, the ability to generate HT bulk samples within a large compositional space and predict the appropriate process conditions for build effectiveness and optimized cooling rate permits useful design capabilities for HT sample fabrication. Specifically, the ability to generate bulk samples with different compositions, validate or refine thermodynamic databases, and provide samples for subsequent characterization and property assessments will enable more discovery in MPEAs.

SUPPLEMENTARY MATERIAL

See Supplementary material for the unknown process parameters development, XRF accuracy and XRD data.

AUTHORS' CONTRIBUTIONS

ZI: Theoretical Dimensionless Number development, Data analysis, Writing - original draft. **PN:** Data Curation, Data analysis, Writing - original draft. **DJT:** Conceptualization, Methodology, Supervision, Resources, Funding acquisition, Project administration, Writing – original draft, review & editing

ACKNOWLEDGEMENT

This work was partially supported by Advanced Research Projects Agency-Energy (ARPA-E) ULTIMATE program (Grant# DE-AR-0001431), ARPA-E (Grant# DE-AR-0001050), and National Science Foundation (NSF) Designing Materials to Revolutionize and Engineer our Future (DMREF) program (Grant #1728933) for the DED powder hoppers.

DECLARATION OF CONFLICTS INTEREST

The authors declare that they have no known competing financial interests or personal relationships that could have appeared to influence the work reported in this paper.

DATA AVAILABILITY

The data that support the findings of this study are available from the corresponding authors upon reasonable request.

REFERENCES

- 1. Cantor B, Chang IT, Knight P, Vincent AJ. Microstructural development in equiatomic multicomponent alloys. Materials Science and Engineering: A. 2004 Jul 1;375:213-8.
- 2. Yeh JW, Chen SK, Lin SJ, Gan JY, Chin TS, Shun TT, Tsau CH, Chang SY. Nanostructured high-entropy alloys with multiple principal elements: novel alloy design concepts and outcomes. Advanced Engineering Materials. 2004 May;6(5):299-303.
- 3. Miracle DB, Senkov ON. A critical review of high entropy alloys and related concepts. Acta Materialia. 2017 Jan 1;122:448-511.
- 4. Miracle DB, Miller JD, Senkov ON, Woodward C, Uchic MD, Tiley J. Exploration and development of high entropy alloys for structural applications. Entropy. 2014 Jan;16(1):494-525.
- 5. Senkov ON, Miller JD, Miracle DB, Woodward C. Accelerated exploration of multiprincipal element alloys with solid solution phases. Nature communications. 2015 Mar 5;6(1):1-0.
- 6. Senkov ON, Miller JD, Miracle DB, Woodward C. Accelerated exploration of multiprincipal element alloys for structural applications. Calphad. 2015 Sep 1;50:32-48.
- 7. Pradeep KG, Tasan CC, Yao MJ, Deng Y, Springer H, Raabe D. Non-equiatomic high entropy alloys: Approach towards rapid alloy screening and property-oriented design. Materials Science and Engineering: A. 2015 Nov 11;648:183-92.
- 8. Ma D, Yao M, Pradeep KG, Tasan CC, Springer H, Raabe D. Phase stability of non-equiatomic CoCrFeMnNi high entropy alloys. Acta Materialia. 2015 Oct 1;98:288-96.
- 9. Shao S, Khonsari MM, Guo S, Meng WJ, Li N. Overview: additive manufacturing enabled accelerated design of Ni-based alloys for improved fatigue life. Additive Manufacturing. 2019 Oct 1;29:100779.
- 10. Moorehead M, Bertsch K, Niezgoda M, Parkin C, Elbakhshwan M, Sridharan K, Zhang C, Thoma D, Couet A. High-throughput synthesis of Mo-Nb-Ta-W high-entropy alloys via additive manufacturing. Materials & Design. 2020 Feb 1;187:108358.
- 11. Vecchio KS, Dippo OF, Kaufmann KR, Liu X. High-Throughput Rapid Experimental Alloy Development (HT-READ). Acta Materialia. 2021 Sep 29:117352.

- 12. Thoma DJ, Charbon C, Lewis GK, Nemec RB. Directed light fabrication of iron-based materials. MRS Online Proceedings Library Archive. 1995;397.
- 13. Elmer JW, Allen SM, Eagar TW. Microstructural development during solidification of stainless steel alloys. Metallurgical transactions A. 1989 Oct 1;20(10):2117-31.
- 14. Zheng B, Zhou Y, Smugeresky JE, Schoenung JM, Lavernia EJ. Thermal behavior and microstructural evolution during laser deposition with laser-engineered net shaping: Part I. Numerical calculations. Metallurgical and materials transactions A. 2008 Sep 1;39(9):2228-36.
- 15. Zheng B, Zhou Y, Smugeresky JE, Schoenung JM, Lavernia EJ. Thermal behavior and microstructure evolution during laser deposition with laser-engineered net shaping: part II. Experimental investigation and discussion. Metallurgical and materials transactions A. 2008 Sep;39(9):2237-45.
- 16. Tsai KY, Tsai MH, Yeh JW. Sluggish diffusion in Co–Cr–Fe–Mn–Ni high-entropy alloys. Acta Materialia. 2013 Aug 1;61(13):4887-97.
- 17. Beke DL, Erdélyi G. On the diffusion in high-entropy alloys. Materials Letters. 2016 Feb 1;164:111-3.
- 18. Wei S, He F, Tasan CC. Metastability in high-entropy alloys: A review. Journal of Materials Research. 2018 Oct;33(19):2924-37.
- 19. Kube SA, Schroers J. Metastability in high entropy alloys. Scripta Materialia. 2020 Sep 1;186:392-400.
- 20. Li Z, Pradeep KG, Deng Y, Raabe D, Tasan CC. Metastable high-entropy dual-phase alloys overcome the strength–ductility trade-off. Nature. 2016 Jun;534(7606):227-30.
- 21. Nene SS, Frank M, Liu K, Mishra RS, McWilliams BA, Cho KC. Extremely high strength and work hardening ability in a metastable high entropy alloy. Scientific reports. 2018 Jul 2;8(1):1-8.
- 22. Van Elsen M, Al-Bender F, Kruth JP. Application of dimensional analysis to selective laser melting. Rapid Prototyping Journal. 2008 Jan 18.
- 23. Wang Z, Liu M. Dimensionless analysis on selective laser melting to predict porosity and track morphology. Journal of Materials Processing Technology. 2019 Nov 1;273:116238.
- 24. Mukherjee T, Manvatkar V, De A, DebRoy T. Dimensionless numbers in additive manufacturing. Journal of Applied Physics. 2017 Feb 14;121(6):064904.
- 25. Rankouhi B, Agrawal AK, Pfefferkorn FE, Thoma DJ. A dimensionless number for predicting universal processing parameter boundaries in metal powder bed additive manufacturing. Manufacturing Letters. 2021 Jan 1;27:13-7.
- 26. Buckingham E. On physically similar systems; illustrations of the use of dimensional equations. Physical review. 1914 Oct 1;4(4):345.
- 27. Wolff SJ, Lin S, Faierson EJ, Liu WK, Wagner GJ, Cao J. A framework to link localized cooling and properties of directed energy deposition (DED)-processed Ti-6Al-4V. Acta Materialia. 2017 Jun 15;132:106-17.
- 28. Rosenthal D. The theory of moving sources of heat and its application of metal treatments. Transactions of ASME. 1946;68:849-66.
- 29. Cverna F, ASMIMPD Committee. ASM Ready Reference: Thermal Properties of Metals, ASM International, 2002.
- 30. Sampson R, Lancaster R, Sutcliffe M, Carswell D, Hauser C, Barras J. An improved methodology of melt pool monitoring of direct energy deposition processes. Optics & Laser Technology. 2020 Jul 1;127:106194.
- 31. Bertsch KM, de Bellefon GM, Kuehl B, Thoma DJ. Origin of dislocation structures in an additively manufactured austenitic stainless steel 316L. Acta Materialia. 2020 Oct 15;199:19-33.
- 32. Kurz W. Fundamentals of solidification. Trans. Tech. Pub.. 1989;194.

- 33. Katayama S, Matsunawa A. Solidification microstructure of laser welded stainless steels. InInternational Congress on Applications of Lasers & Electro-Optics 1984 Nov (Vol. 1984, No. 2, pp. 60-67). Laser Institute of America.
- 34. Agrawal AK, de Bellefon GM, Thoma D. High-throughput experimentation for microstructural design in additively manufactured 316L stainless steel. Materials Science and Engineering: A. 2020 Aug 19;793:139841.

Supplementary Document

A Dimensionless Number for High-throughput Design of Multi-Principal Element Alloys in Directed Energy Deposition

Zahabul Islam, Phalgun Nelaturu, Dan J. Thomaa)

AFFILIATIONS

Alloy Design and Development Laboratory, Department of Materials Science and Engineering, University of Wisconsin, Madison, WI 53706, USA

a) Author to whom correspondence should be addressed: dthoma@wisc.edu

S1: Development of unknown process parameters using the dimensionless number:

Unknown process parameters of a material can be determined using the dimensionless number, Π_2 and the linear fit represented by Eq. 8 (in the manuscript). For example, at a dimensionless number $\Pi_2 = 90$, using Eq. 8 (in the manuscript), the mass flow rate can be calculated as 5.56 gm/min. Now by setting $\frac{h_{actutal}}{(n \times Z)} \approx 1$ a high throughput (HT) process parameters test matrix using Eqs. (3), (6) and (8) can be developed.

The following section shows how the dimensionless number can be used to define the high throughput process parameters test matrix for molybdenum and copper. During the printing process laser power, feed rate, hatch spacing, and layer thickness were varied while a bi-directional, a single pass of the laser beam, and a 90° rotation of scan vector scan strategy was kept constant. Using the linear fit in Fig. 4 mentioned in the manuscript (Fig. 1s in the supplementary section) we can calculate the HT process parameters for molybdenum and copper as follows:

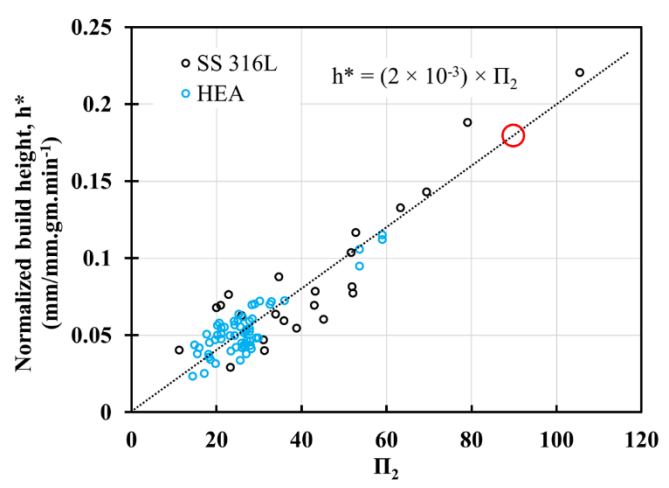


Fig. 1s: Normalized build height vs Dimensionless number

$$h^* = 2 \times 10^{-3} \times \Pi_2 \tag{1s}$$

To maintain geometric dimensional accuracy, ratio of actual build height to the set build height has to be approximately 1. Mathematically this can be written as follow:

$$\frac{h_{actutal}}{(n \times Z)} \approx 1$$
 (2s)

Now, if Π_2 is chosen as 90 as shown in Fig. 1s (red circle), and using Eqs. 1s, 2s, and 3s mass flow rate can be calculated as shown by Eq. 4s.

$$h^* = \frac{h_{actutal}}{(n \times Z) \times \dot{m}} = 2 \times 10^{-3} \times 90$$
 (3s)

$$\dot{m} = 5.56 \text{ gm/min} \tag{4s}$$

Now the dimensionless number can be written as follows:

$$\Pi_2 = \frac{E_g \times \alpha}{\dot{m} \times H} \times \frac{Z}{h} = \frac{P \times \alpha}{\nu \times D_t \times \dot{m} \times H} \times \frac{Z}{h} = 90$$
 (5s)

To define the HT process parameters for a new material like molybdenum (a high-temperature material) as a test case, Eq. 5s can be used. Using molybdenum thermo-physical properties (Table II), α =53.8 mm²/s, H_f = 375.2 kJ/kg, C_p =0.251 kJ.kg¹-I.K¹-I, T_m = 2896K, and laser spot diameter, D_l = 0.6mm, a relationship between process parameters can be developed as follows:

$$\Pi_2 = \frac{P \times 53.8}{\nu \times 0.6 \times \left(\frac{5.56}{60}\right) \times [375.2 + \{0.251 \times (2896 - 298)\}]} \times \frac{Z}{h} = 90$$
(6s)

$$\frac{P}{v} \times \frac{Z}{h} = 96 \tag{7s}$$

By setting layer thickness and hatch spacing as 0.01 inch, and using Eq. 7s laser power can be determined as P = 650W at a feed rate of v = 16 inch/min. It is expected that using these process parameters i.e., P = 650W, v = 16in/min, Z = 0.01 inch, and h = 0.01 inch predicted dimensional accuracy can be achieved.

By following the same procedure, a test matrix for a high thermal conductive material such as copper can be also developed. Using the thermo-physical properties of Copper (Table. II), α =111 mm²/s, H_f = 206 kJ/kg, C_p =0.385 kJ.kg⁻¹.K⁻¹, T_m = 1358K, and laser spot diameter, D_l = 0.6mm process parameters from Eq. 5s for Copper can be estimated as P=355W, v=20in/min, Z=0.01 inch, and h=0.015 inch.

The following TABLE S.I shows high throughput process parameters test matrix for molybdenum and copper obtained from dimensionless number:

TABLE S.I. Table showing the process parameters predicted using Eqs. (3), (6), and (8):

Materials	Laser power (W)	Feed rate (mm/s)	Layer thickness (mm)	Hatch spacing (mm)	Mass flow rate (g/min)
Mo	600-700	5-10	0.25-0.5	0.25-0.5	5-12
Cu	225-500	7-15	0.25-0.75	0.25-0.75	5-15

S2: Accuracy of XRF compositions:

A 316L SS specimen was used to calibrate the accuracy of the XRF measurements. The actual compositions were measured by Luvak, Inc. Carbon and sulfur contents were measured using combustion infrared detection based on ASTM E 1019-18. All other element contents were measured using direct current plasma emission spectroscopy based on ASTM E 1097-12. The comparison of the XRF-measured composition of the 316L standard against that measured by Luvak is given in Table S.II.

TABLE S.II. Comparison of XRF compositions vs. Luvak-measured compositions of the 316L standard specimen. Note that the XRF is unable to measure trace amounts of the low atomic weight elements).

Element	Luvak compositions (wt%)	XRF compositions (wt%)
Fe	66.8253 ± 0.5	67.11 ± 0.83
Cr	16.8 ± 0.3	17.08 ± 0.2
Ni	12.2 ± 0.2	12.08 ± 0.15
Mo	2.49 ± 0.04	2.53 ± 0.025
Mn	1.19 ± 0.02	1.19 ± 0.05
Si	0.4 ± 0.01	
N	0.053 ± 0.002	
O	0.026 ± 0.001	
C	0.005 ± 0.0005	
S	0.005 ± 0.0005	
P	0.0039 ± 0.0005	
Н	0.0008 ± 0.0005	
Al	$< 0.0005 \pm 0.0005$	
Ti	$< 0.0005 \pm 0.0005$	

S3: XRD of single-phase FCC alloy:

The phases present in all the alloy samples were measured via automated X-ray diffraction (XRD) in a Bruker D8 Discovery X-ray diffractometer. The pattern obtained for the single-phase FCC alloy of nominal composition $Fe_{60}Ni_{20}Cr_{10}Mo_{10}$ is shown below:

